MODELLISTICA E CALCOLO SCIENTIFICO

MOX

MODELING AND SCIENTIFIC COMPUTING

MOX-Report No. 11/2015

High order discontinuous Galerkin methods on simplicial elements for the elastodynamics equation

Antonietti, P. F.; Marcati, C.; Mazzieri, I.; Quarteroni, A.

High order discontinuous Galerkin methods on simplicial elements for the elastodynamics equation

Paola F. Antonietti[♭], Carlo Marcati[§,◊], Ilario Mazzieri[♭], and Alfio Quarteroni[♯]

February 23, 2015

[♭] MOX, Dipartimento di Matematica, Politecnico di Milano
Piazza Leonardo da Vinci 32, I-20133 Milano, Italy.
`paola.antonietti@polimi.it`, `ilario.mazzieri@polimi.it`

[§] Sorbonne Universités, UPMC Univ Paris 06, UMR 7598, Laboratoire Jacques-Louis Lions,
F-75005, Paris, France. `carlo.marcati@upmc.fr`

[◊] CNRS, UMR 7598, Laboratoire Jacques-Louis Lions, F-75005, Paris, France.

[♯] CMCS, École Polytechnique Fédérale de Lausanne (EPFL), Station 8, 1015 Lausanne,
Switzerland. `alfio.quarteroni@epfl.ch`

Abstract

In this work apply the discontinuous Galekin (dG) spectral element method on meshes made of simplicial elements for the approximation of the elastodynamics equation. Our approach combines the high accuracy of spectral methods, the geometrical flexibility of simplicial elements and the computational flexibility of dG methods. We analyze the dissipation, dispersion and stability properties of the resulting scheme, with a focus on the choice of different sets of basis functions. Finally, we test the method on benchmark as well as realistic test cases.

Keywords: Spectral methods; Discontinuous Galerkin; Simplicial elements; Computational seismology; Numerical approximations and analysis

1   Introduction

In many geophysical research fields as, for example, seismic exploration, volcano seismology, seismic tomography, rupture mechanics and seismic hazard analysis, advanced numerical strategies provide an effective tool for data analysis, early warning and planning purposes and can enhance the mitigation of hazards and decreasing the risk near densely urbanized areas. Recently, discontinuous Galerkin (dG) spectral element methods on tensor product elements have become very attractive for the simulation of wave propagation and have found remarkable applications in geophysics owing to the ever increasing progress in computer algorithms and large-scale computing facilities.

Spectral element methods have been introduced in 1984 by Patera [34] for computational fluid dynamics and are nowadays well-established techniques for the approximation of partial differential equations [10]. In the last two decades, they have been extensively used in the context of computational seismology, e.g., [26, 36, 16, 44, 46], where both high order accuracy and computational efficiency are mandatory. In the early days, spectral element methods were invariably used on meshes made of tensor product elements (i.e.,

affine deformed squares and cubes) since this is the context in which the extension from one spatial dimension to two or three dimensions naturally occurs [9]. Their extension to triangles and tetrahedra (see [24, 45]) has been historically less developed, and different approaches have been proposed and analysed in the last years, see again [24] and e.g, [43, 23]. Several of these formulations have been employed for seismic wave propagation, e.g., [32, 35].

On their side, discontinuous Galerkin methods for the solution of partial differential equations have been greatly developed since they were first introduced in the seventies for the numerical approximation of hyperbolic problems [40] and, independently, in the context of elliptic and parabolic equations [4, 13]. See [5] for a unified review of dG methods for elliptic problems. Combining the best of both the finite elements and the finite volumes methods, they exhibit many interesting properties and they are highly scalable and flexible. On one hand, since many algorithmic operations take place at the element level, dG methods are well suited for highly parallel environments [25]. On the other hand, they can handle naturally non-matching grids and variable approximation orders. Such flexibility has been successfully exploited in conjunction with spectral element methods in the context of elastodynamics problems, on tensor product grids [30].

In this work, we analyze the discontinuous Galerkin spectral element method (dGSEM) on simplicial meshes for the approximation of seismic wave propagation in heterogeneous media. We consider two different approaches for the construction of the element-wise discrete space: the former exploits modal Legendre-Dubiner basis functions [14, 27] and can be used in the framework of a fully discontinuous approximation, since there is no way to impose the continuity of the approximation space with these shape functions. The latter approach is based on boundary adapted nodal basis functions [10, 14, 24], suitably modified to allow for a continuous scheme.

The paper is organized as follows. In Section 2 we introduce the model problem; we discuss its numerical discretization in Section 3. Starting from the work presented in [31], we derive in Section 4 a thorough analysis of the dispersion and dissipation errors introduced by the numerical method. Low dispersion and dissipation errors are indeed relevant in order to accurately approximate fast waves in extended domains. Furthermore, the requirements for the numerical stability of the method (of computational relevance) are investigated and the convergence properties of the method are verified. Then, the method is applied to some classical seismic wave propagation problems in Section 5. Finally, conclusions and perspectives are drawn in Section 6.

The results we obtained show that the dGSEM on simplicial elements provides a highly accurate and rapidly convergent approximation. We are also able to quantify the low dispersion and dissipation errors introduced, as well as the stability requirements of the method.

Throughout the paper, we use the standard notation for Sobolev spaces [1]. For a bounded domain $D \subset \mathbb{R}^d$, $d = 2, 3$, we denote by $H^m(D)$ the L^2-Sobolev space of order $m \geq 0$ and by $\|\cdot\|_{m,D}$ and $|\cdot|_{m,D}$ the usual Sobolev norm and seminorm, respectively. For $m = 0$, we write $L^2(D)$ instead of $H^0(D)$. The space $H^1_{0,\Gamma}(D)$ is the subspace of $H^1(D)$ of functions with zero trace on $\Gamma \subseteq \partial D$. Due to the nature of the problem, we write in boldface vector-valued functions. Finally, we write $a \approx b$ if there exists two positive constants C_1 and C_2 that do not depend on the discretization parameters such that $C_1 a \leq b \leq C_2 a$.

2   The mathematical model

Let Ω be a sufficiently smooth bounded region of $\mathbb{R}^d$, $d = 2, 3$ and let Γ be its boundary with outward normal unit vector $\mathbf{n}$. We suppose that Γ is subdivided into a part Γ_D, where Dirichlet conditions (i.e., displacements) are prescribed, and a part Γ_N, where Neumann conditions (i.e., surface loads) are imposed. We suppose that Γ_D and Γ_N are non overlapping, i.e., $\Gamma_D \cap \Gamma_N = \emptyset$, and that Γ_N can be empty. Given a final observation time $T > 0$, the linear elastodynamics equation takes the form:

$$
\begin{cases}
\rho \mathbf{u}_{tt} - \nabla \cdot \sigma(\mathbf{u}) = \mathbf{f}, & \text{in } \Omega \times (0, T], \\
\mathbf{u} = \mathbf{0}, & \text{on } \Gamma_D \times (0, T], \\
\sigma(\mathbf{u})\mathbf{n} = \mathbf{g}, & \text{on } \Gamma_N \times (0, T], \\
\mathbf{u} = \mathbf{u_0}, & \text{in } \Omega \times \{0\}, \\
\mathbf{u}_t = \mathbf{v_0}, & \text{in } \Omega \times \{0\}.
\end{cases}
\tag{1}
$$

Here, $\mathbf{u}$ represents the displacement of the body, $\rho > 0$ the medium mass density and $\mathbf{f}, \mathbf{g}$ assigned loads. We define the strain tensor $\varepsilon(\mathbf{u}) = \frac{1}{2}\left(\nabla \mathbf{u} + \nabla \mathbf{u}^\top\right)$, and we consider the stress tensor σ for a linear isotropic elastic medium prescribed by the *Hooke's law*, given component-wise by

$$
\sigma_{ij}(\mathbf{u}) := \sum_{k,\ell=1}^{d} \mathbb{C}_{ijk\ell}\, \varepsilon_{k\ell}(\mathbf{u}), \quad \text{for } i, j = 1, ..., d,
\tag{2}
$$

where $\mathbb{C}$ is the stiffness fourth order tensor. For isotropic media, relation (2) reduces to

$$
\sigma_{ij}(\mathbf{u}) := \lambda \sum_{k=1}^{d} \varepsilon_{kk}(\mathbf{u})\delta_{ij} + 2\mu\varepsilon_{ij}(\mathbf{u}) \quad \text{for } i, j = 1, ..., d,
$$

where λ and μ are referred to as the first and second Lamé parameter, respectively. We assume the parameters ρ, λ and μ to be piece-wise positive constant functions, therefore $\rho, \lambda, \mu \in L^\infty(\Omega)$. Under these hypotheses, we remark that the stiffness tensor $\mathbb{C}$ is positive definite and satisfies the bounds

$$
2\mu \sum_{i,j=1}^{d} x_{ij}x_{ij} \leq \sum_{i,j,k,\ell=1}^{d} x_{ij}\mathbb{C}_{ijk\ell}\, x_{k\ell} \leq 2(\lambda + \mu) \sum_{i,j=1}^{d} x_{ij}x_{ij} \quad \forall x \in \mathbb{R}^{d \times d}.
$$

Here and in the sequel we define the speed of a compressional and shear wave as $c_P := \sqrt{(\lambda + 2\mu)/\rho}$ and $c_S := \sqrt{\mu/\rho}$.

Next, we consider the variational formulation of (1): for all $t \in (0, T]$ find $\mathbf{u} = \mathbf{u}(t) \in \boldsymbol{H}_{0,\Gamma_D}^1(\Omega)$ such that:

$$
(\rho \mathbf{u}_{tt}, \mathbf{v})_\Omega + \mathcal{A}(\mathbf{u}, \mathbf{v}) = \mathcal{F}(\mathbf{v}) \qquad \forall \mathbf{v} \in \boldsymbol{H}_{0,\Gamma_D}^1(\Omega),
\tag{3}
$$

with $\mathbf{u}(0) = \mathbf{u}_0$ and $\mathbf{u}_t(0) = \mathbf{v}_0$. Here, $\mathcal{A}(\cdot, \cdot) : \boldsymbol{H}_{0,\Gamma_D}^1(\Omega) \times \boldsymbol{H}_{0,\Gamma_D}^1(\Omega) \to \mathbb{R}$ is defined by

$$
\mathcal{A}(\mathbf{u}, \mathbf{v}) := (\sigma(\mathbf{u}), \varepsilon(\mathbf{v}))_\Omega,
$$

and $\mathcal{F} : \boldsymbol{H}_{0,\Gamma_D}^1(\Omega) \to \mathbb{R}$ by

$$
\mathcal{F}(\mathbf{v}) := (\mathbf{f}, \mathbf{v})_\Omega + (\mathbf{g}, \mathbf{v})_{\Gamma_N}.
$$

The following well posedness result holds, cf. [39].

Lemma 2.1. *If $\mathbf{u}_0 \in \boldsymbol{H}_{0,\Gamma_D}^1(\Omega)$, $\mathbf{v}_0 \in \boldsymbol{L}^2(\Omega)$, $\mathbf{f} \in L^2((0, T]; \boldsymbol{L}^2(\Omega))$ and $\boldsymbol{g} \in C^1((0, T]; \boldsymbol{H}^{1/2}(\Gamma_N))$, then problem (3) admits a unique solution $\mathbf{u} \in C((0, T]; \boldsymbol{H}_{0,\Gamma_D}^1(\Omega)) \cap C^1((0, T]; \boldsymbol{L}^2(\Omega))$.*

3 Numerical approximation

In this section, we describe the numerical method employed for the approximation of (1). After introducing the basic notation, we derive the corresponding semidiscrete and fully-discrete formulation, giving particular emphasis to the choice of the basis function and the quadrature rules adopted in this framework.

3.1 Space discretization

Let us consider a family $\{\mathcal{T}_h, 0 < h \leq 1\}$ of shape-regular conforming triangulations of Ω made of disjoint open elements K such that $\overline{\Omega} = \cup_{K \in \mathcal{T}_h} \overline{K}$, where each $K \in \mathcal{T}_h$ is the image of a fixed master d-simplicial element $\widehat{K} \in \mathbb{R}^d$, $d = 2, 3$, i.e., $K = F_K(\widehat{K})$. We define the mesh size of $\mathcal{T}_h$ as $h = \max_{K \in \mathcal{T}_h} h_K$ with $h_K = \mathrm{diam}(K)$. We define an interior face of $\mathcal{T}_h$ (edge for $d = 2$) as the non–empty interior of $\partial \overline{K}^+ \cap \partial \overline{K}^-$, where K^+ and K^- are two adjacent elements of $\mathcal{T}_h$. Similarly, a boundary face of $\mathcal{T}_h$ is defined as the non–empty interior of $\partial \overline{K} \cap \overline{\Omega}$, where K is a boundary element of $\mathcal{T}_h$. We collect all the interior (resp. boundary) faces in the set $\mathcal{E}_h^I$ (resp. $\mathcal{E}_h^\partial$) and set $\mathcal{E}_h = \mathcal{E}_h^I \cup \mathcal{E}_h^\partial$. In particular $\mathcal{E}^\partial = \mathcal{E}^D \cup \mathcal{E}^N$, where $\mathcal{E}^D$ and $\mathcal{E}^N$ contain all Dirichlet and Neumann boundary faces, respectively. Moreover we implicitly assume that the triangulation $\mathcal{T}_h$ respects the decomposition of $\partial \Omega$, i.e., any $e \in \mathcal{E}^\partial$ belongs to the interior of exactly one of $\mathcal{E}^D$ or $\mathcal{E}^N$. Finally, we suppose that for any pair of elements K^+ and K^- sharing a $(d-1)$–dimensional face $h_{K^+} \approx h_{K^-}$ (cf. [18, 19]).

Next, we introduce the average $\{\!\{\cdot\}\!\}$ and jump $[\![\cdot]\!]$ operators for vector-valued and tensor-valued functions. For any face $e \in \mathcal{E}_h^I$, shared by two neighbouring elements K^+ and K^-, we define

$$[\![\mathbf{u}]\!] := \mathbf{u}^+ \otimes \mathbf{n}^+ + \mathbf{u}^- \otimes \mathbf{n}^-, \quad [\![\sigma(\mathbf{u})]\!] := \sigma(\mathbf{u}^+)\mathbf{n}^+ + \sigma(\mathbf{u}^-)\mathbf{n}^-,$$

$$\{\!\{\mathbf{u}\}\!\} := \frac{1}{2}(\mathbf{u}^+ + \mathbf{u}^-), \qquad \{\!\{\sigma(\mathbf{u})\}\!\} := \frac{1}{2}(\sigma(\mathbf{u}^+) + \sigma(\mathbf{u}^-)),$$

where $\mathbf{n}^+$ (resp. $\mathbf{n}^+$) is the outward normal unit vector to K^+ (resp. K^-) and $\mathbf{a} \otimes \mathbf{b} \in \mathbb{R}^{d \times d}$ is the tensor whose entries are $(\mathbf{a} \otimes \mathbf{b})_{ij} = a_i b_j$ for $i, j = 1, ..., d$. For any boundary edge $e \in \mathcal{E}^\partial$ we define

$$\{\!\{\mathbf{u}\}\!\} := \mathbf{u}, \qquad \{\!\{\sigma(\mathbf{u})\}\!\} := \sigma(\mathbf{u}), \qquad [\![\mathbf{u}]\!] = \mathbf{u} \otimes \mathbf{n}, \qquad [\![\sigma(\mathbf{u})]\!] = \sigma(\mathbf{u})\mathbf{n}.$$

Finally, for any $p > 0$, we consider the finite-dimensional approximation space

$$\boldsymbol{V}^h := \{\mathbf{v} \in \boldsymbol{L}^2(\Omega) : \mathbf{v} \circ F_K \in \mathbb{P}^p(\widehat{K}) \quad \forall \, K \in \mathcal{T}_h\},$$

where $\mathbb{P}^p(\widehat{K})$ is the space of polynomials of total degree at most p on $\widehat{K}$.

In order to recast all the Interior Penalty (IP) schemes in a unique variational formulation we introduce the following bilinear forms. Let $H^m(\mathcal{T}_h)$ be the Sobolev space of piecewise H^m functions, $m > 3/2$, we define $\mathcal{B} : \boldsymbol{H}^m(\mathcal{T}_h) \times \boldsymbol{H}^m(\mathcal{T}_h) \to \mathbb{R}$ as

$$\mathcal{B}(\mathbf{u}, \mathbf{v}) := \sum_{K \in \mathcal{T}_h} \mathcal{A}_K(\mathbf{u}, \mathbf{v}) + \sum_{e \in \mathcal{E}} \mathcal{I}_e(\mathbf{u}, \mathbf{v}) + \sum_{e \in \mathcal{E}^I \cup \mathcal{E}^D} \mathcal{S}_e(\mathbf{u}, \mathbf{v}), \tag{4}$$

where $\mathcal{A}_K$ is the restriction of $\mathcal{A}$ to the element K, i.e., $\mathcal{A}_K(\mathbf{u}, \mathbf{v}) := (\sigma(\mathbf{u}), \varepsilon(\mathbf{v}))_K$, $\mathcal{I}_e$ is defined by

$$\mathcal{I}_e(\mathbf{u}, \mathbf{v}) := - (\{\!\{\sigma(\mathbf{u})\}\!\}, [\![\mathbf{v}]\!])_e - \eta (\{\!\{\sigma(\mathbf{v})\}\!\}, [\![\mathbf{u}]\!])_e \tag{5}$$

4

for $\eta \in \{-1, 0, 1\}$, and $\mathcal{S}_e$ by

$$\mathcal{S}_e(\mathbf{u}, \mathbf{v}) := (\mathbb{S}_e[\![\mathbf{u}]\!], [\![\mathbf{v}]\!])_e, \tag{6}$$

where

$$\mathbb{S}_e := \alpha h_e^{-1} p^2 \{\mathbb{C}\}_H \qquad \forall e \in \mathcal{E}^I \cup \mathcal{E}^D, \tag{7}$$

is the penalty function, α is a strictly positive constant and $\{a\}_H$ is the harmonic average of the quantity a, i.e., $\{a\}_H := 2a^+a^-/(a^+ + a^-)$. For tensor-valued functions the harmonic average is meant to be applied component-wise. We remark that other penalty functions can be selected for the term (6) as, for instance, the one proposed in [3, 41]:

$$\mathbb{S}_e := \alpha h_e^{-1} k^2 \{(\lambda + 2\mu)\mathbb{I}\}_H \qquad \forall e \in \mathcal{E}^I \cup \mathcal{E}^D, \tag{8}$$

being $\mathbb{I}$ the identity tensor.

The semidiscrete approximation of (1) is then given by: for all $t \in (0, T]$ find $\mathbf{u}^h = \mathbf{u}^h(t) \in \boldsymbol{V}^h$ such that:

$$(\rho \mathbf{u}_{tt}^h, \mathbf{v})_\Omega + \mathcal{B}(\mathbf{u}^h, \mathbf{v}) = \mathcal{F}(\mathbf{v}) \qquad \forall \mathbf{v} \in \boldsymbol{V}^h. \tag{9}$$

Notice that with $\eta = 1$ in (5) we obtain the Symmetric Interior Penalty (SIP) method [4, 51], with $\eta = -1$ the Non-symmetric Interior Penalty (NIP) method [42] and with $\eta = 0$ the Incomplete Interior Penalty (IIP) method [51]. Employing standard techniques it is possible to prove that problem (9) is well posed. Moreover, optimal a-priori error bounds can be drawn for the semidiscrete solution $\mathbf{u}^h$, see [6] for further details.

We next fix a basis for V_h (whose precise definition will be discussed in Section 3.3) and rewrite (9) as a system of ordinary differential equations. To ease the reading, here and in the following we discuss the case $\Omega \subset \mathbb{R}^2$; the extension to $d = 3$ is straightforward. We start defining on every triangle $K \in \mathcal{T}_h$ the basis functions $\{\boldsymbol{\psi}_i^\ell\}_i^{\ell=1,2}$ by setting

$$\boldsymbol{\psi}_i^1 := \begin{pmatrix} \psi_i \\ 0 \end{pmatrix}, \qquad \boldsymbol{\psi}_i^2 := \begin{pmatrix} 0 \\ \psi_i \end{pmatrix},$$

where $\{\psi_i\}_i$ is a basis for V_h on K. We denote by $N_p = (p+1)(p+2)/2$ the number of degrees of freedom per element and by n_{el} the number of elements of $\mathcal{T}_h$. The total number of degrees of freedom per component is thus $N_{tot} = N_p n_{el}$. Therefore, the trial function $\mathbf{u}_h$ can be expanded as

$$\mathbf{u}_h = \sum_{j=0}^{n_{el}-1} \sum_{i=jN_p+1}^{jN_p+N_p} \left(u_i^1 \boldsymbol{\psi}_i^1 + u_i^2 \boldsymbol{\psi}_i^2 \right).$$

Writing (4) for any test function $\{\boldsymbol{\psi}_i^\ell\}_{\ell=1,2}$ in $\boldsymbol{V}^h$, we obtain the following system of second order ordinary differential equation

$$M\ddot{\mathbf{U}} + (A + J + S)\mathbf{U} = \mathbf{F} \tag{10}$$

for the unknowns $\mathbf{U} = \left(u_1^1, ..., u_{N_{tot}}^1, u_1^2, ..., u_{N_{tot}}^2 \right)^\top$, where M is the mass matrix and A, J and S are the matrix representations of the bilinear forms $\mathcal{A}$, $\mathcal{I}$ and $\mathcal{S}$, respectively. Now, let us decompose any of the matrices M, A, J and S in (10) into four blocks of the form

$$C = \begin{pmatrix} C^{11} & C^{12} \\ C^{21} & C^{22} \end{pmatrix}, \quad \text{for } C = M, A, J, S.$$

Since we are considering an element-wise discontinuous basis, M is block diagonal, i.e. $M^{12} = M^{21} = 0$, while M^{ii} $i = 1, 2$ are composed of n_{el} diagonal blocks of size $N_p \times N_p$.
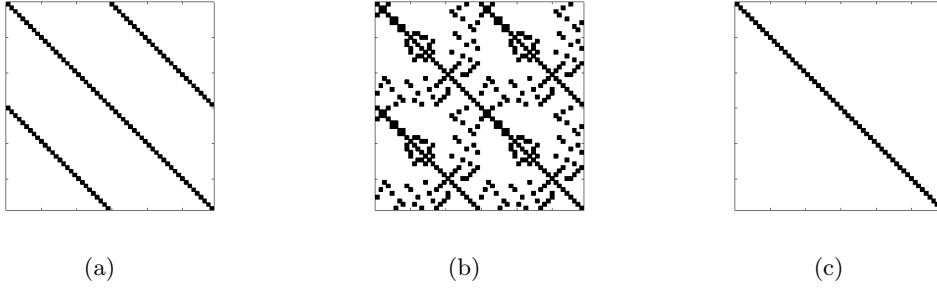
Figure 1: Sparsity patterns for (a) A, (b) J and (c) M on a conforming mesh.

The four blocks A^{ij} of A exhibit the same block diagonal structure of M^{ii}, so that the matrix has a main block diagonal and two smaller ones in the A^{12} and A^{21} blocks.

The sparsity pattern of J is the same for all the sub-blocks, with every row and column related to the element K containing a N_p by N_p block in diagonal position and $\#\{e \in \partial K \cap \mathcal{E}^I\}$ non-diagonal blocks.

The matrix S has the same pattern as J if the penalty function is defined as in (7). Otherwise, if it is formulated as in (8), S^{ii}, $i = 1, 2$, have the same structure of J^{ij}, but $S^{12} = S^{21} = 0$. An example of those patterns is given in Figure 1, where an approximation with polynomial degree $p = 5$ and $N_{el} = 28$ elements are considered.

Next, we identify by A_K (resp. M_K) the sub-block of A (resp. M) corresponding to the element K and by $J_{K,L}$ and $S_{K,L}$ the blocks of the inter-element and stability matrices corresponding to the edge of K whose neighbour is the element L. Therefore,

$$A_K^{\ell m}[i,j] = \mathcal{A}_K(\boldsymbol{\psi}_j^m, \boldsymbol{\psi}_i^\ell) \quad \text{for } \ell, m = 1, 2,$$

and

$$M_K^{\ell \ell}[i,j] = (\rho \psi_j^\ell, \psi_i^\ell)_K \quad \text{for } \ell = 1, 2.$$

Similarly,

$$J_{K,L}^{\ell m}[i,j] = \mathcal{I}_e(\boldsymbol{\psi}_j^m, \boldsymbol{\psi}_i^\ell) \quad \text{and} \quad S_{K,L}^{\ell m}[i,j] = \mathcal{S}_e(\boldsymbol{\psi}_j^m, \boldsymbol{\psi}_i^\ell) \quad \text{for } \ell, m = 1, 2,$$

with $e = \partial K \cap \partial L$.

3.2 Time discretization

To integrate in time problem (10), we first subdivide the interval $(0, T]$ in S subintervals of amplitude $\Delta t = T/S$, set $t_n = n\Delta t$ for $n = 0, ..., S$ and denote by $\mathbf{U}_n = \mathbf{U}(t_n)$. Then, setting $D = A + J + S$ and applying the leap-frog method [37], we get

$$M\mathbf{U}_1 = \left(M - \frac{\Delta t^2}{2}D\right)\mathbf{U}_0 - \Delta t M\mathbf{V}_0 + \frac{\Delta t^2}{2}\mathbf{F}_0, \tag{11}$$

for the first step, and

$$M\mathbf{U}_{n+1} = \left(2M - \Delta t^2 D\right)\mathbf{U}_n - M\mathbf{U}_{n-1} + \Delta t^2 \mathbf{F}_n, \quad \text{for } n = 1, ..., S - 1. \tag{12}$$

We recall that the time integration scheme (11)–(12), belongs to the family of Newmark methods, it is explicit and second order accurate. The numerical stability of the method
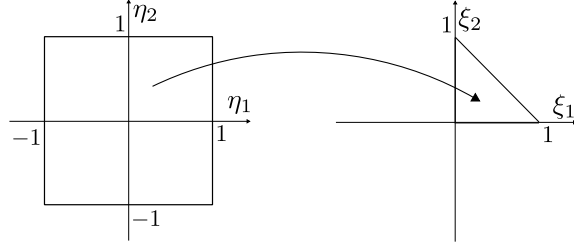
6

Figure 2: The mapping from the reference square $\mathcal{Q}$ to the reference triangle $\mathcal{T}$.

is guaranteed by the Courant-Friedrichs-Lewy (CFL) condition [11], that imposes the following restriction on the time step Δt, i.e.,

$$\Delta t \leq C_{CFL} \frac{\min_{K \in \mathcal{T}_h} h_K}{c_P}, \tag{13}$$

for $0 < C_{CFL} \leq 1$.

3.3 Construction of the element-wise discrete space

In this section we discuss in detail how to construct a set of shape functions to span the discrete space at the element-wise level. Consider the reference square $\widehat{\mathcal{Q}} = \{(\eta_1, \eta_2) : -1 \leq \eta_2, \eta_2 \leq 1\}$, and the reference triangle

$$\widehat{\mathcal{T}} = \{(\xi_1, \xi_2) : \xi_1, \xi_2 \geq 0, \ \xi_1 + \xi_2 \leq 1\}$$

that can be derived from $\widehat{\mathcal{Q}}$ via the transformation map

$$\xi_1 = \frac{(1 + \eta_1)(1 - \eta_2)}{4}, \qquad \xi_2 = \frac{1 + \eta_2}{2}, \tag{14}$$

shown in Figure 2. The inverse map, often referred to as the *Duffy's transformation*, explicitly given by

$$\eta_1 = 2\frac{\xi_1}{1 - \xi_2} - 1, \qquad \eta_2 = 2\xi_2 - 1,$$

is singular at the top vertex of the triangle. The map (14) is indeed "collapsing" the square's edge, identified by $\eta_2 = 1$, onto that single vertex.

The first approach for the construction of the discrete space that we consider is based on a *modal expansion*. The idea is to employ the Jacobi polynomials $J_n^{\alpha,\beta}$ (see [47, 9]) to construct an orthogonal basis which still exhibits a tensor product structure. The orthogonal basis $\{\psi_{ij}(\xi_1, \xi_2)\}_{ij}$, first introduced by Koornwinder [27] and then developed by Dubiner [14], takes the form

$$\psi_{ij}(x, y) = c_{ij}\varphi_i(\eta_1)\varphi_{ij}(\eta_2) = c_{ij}\varphi_i\left(2\frac{\xi_1}{1 - \xi_2} - 1\right)\varphi_{ij}\left(2\xi_2 - 1\right), \tag{15}$$

for $i, j \geq 0$, with $i + j \leq p$ and where

$$c_{ij} = \sqrt{2(2i + 1)(i + j + 1)}, \quad \varphi_i(x) = J_i^{0,0}(x) \quad \text{and} \quad \varphi_{ij}(x) = (1 - x)^j J_j^{2i+1,0}(x).$$

In the second approach we consider, the basis defined in (15) is modified in order to build a $\mathcal{C}^0$ continuous expansion, while retaining some of the advantages provided by Jacobi polynomials. The modes in the modified basis, presented e.g. in [45, 14], can be divided
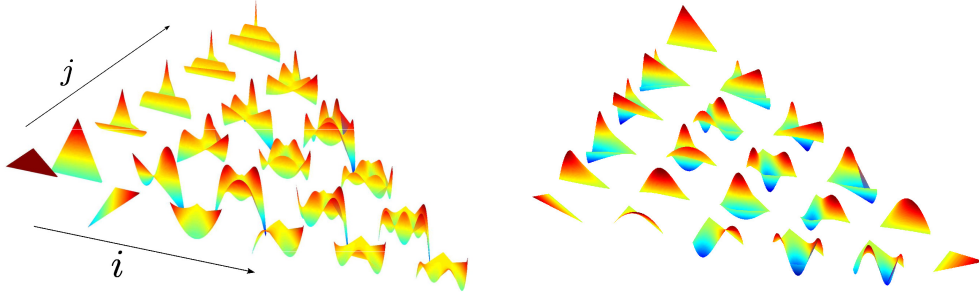
7

Figure 3: Left: Dubiner basis (15). Right: Boundary adapted basis: vertex modes are represented at the corners and edge modes on the edges.

into vertex modes (which are null on two vertex and take a unitary value on the other), boundary modes (which are null on all edges except one) and interior modes (which are null on all edges of the triangle). Both the Dubiner and the modified bases are represented in Figure 3. The modified basis will be identified in the sequel also as boundary adapted basis. In particular, given the reference triangle $\mathcal{T}$, if p is the polynomial degree of the basis, the vertex modes are

$$\psi_1 = 1 - \xi_1 - \xi_2, \quad \psi_2 = \xi_1, \quad \psi_3 = \xi_2,$$

the boundary modes are

$$
\begin{aligned}
\psi_{m(i)} &= (1 - \xi_1 - \xi_2)\,\xi_1\,(1 - \xi_2)^{i-1}\,J_{i-1}^{1,1}\left(\frac{2\xi_1}{1 - \xi_2} - 1\right), \\
\psi_{n(i)} &= (1 - \xi_1 - \xi_2)\,\xi_2 J_{i-1}^{1,1}\left(2\xi_2 - 1\right), \\
\psi_{o(i)} &= \xi_1 \xi_2 J_{i-1}^{1,1}\left(2\xi_2 - 1\right),
\end{aligned}
$$

for $i = 1, \ldots, p - 1$ and the internal modes are

$$\psi_{p(i,j)} = (1 - \xi_1 - \xi_2)\,\xi_1 \xi_2\,(1 - \xi_2)^{i-1}\,J_{i-1}^{1,1}\left(\frac{2\xi_1}{1 - \xi_2} - 1\right) J_{j-1}^{2i+1,1}\left(2\xi_2 - 1\right),$$

for $1 \leq i, j \leq p - 1$, $i + j \leq p - 1$. Here, m, n, o and p are bijections that put the basis in the desired order, see Figure 3.

A different kind of basis, not considered in this work, is the nodal basis, based on a set of interpolation nodes and on the Lagrange functions associated with them, see [23]. The choice of a good set of interpolation points is an open problem, especially in $d = 3$ dimensions, see for instance [17, 21, 22, 33, 38, 50]. Note that Gauss nodes are also Fekete nodes on the square [8], while they differ on the triangle. A full description of nodal bases is beyond the scope of this work; their advantage resides mainly in the possibility to build a continuous approximation, even when dealing with meshes composed of elements of different shape.

We conclude this section discussing the quadrature rules we are going to employ. The standard approach is to map the Gauss quadrature nodes from quadrilateral elements to triangular ones employing the transformation (14). The degree of exactness of these rules is thus preserved, but none of the symmetries of the triangle are considered and the points
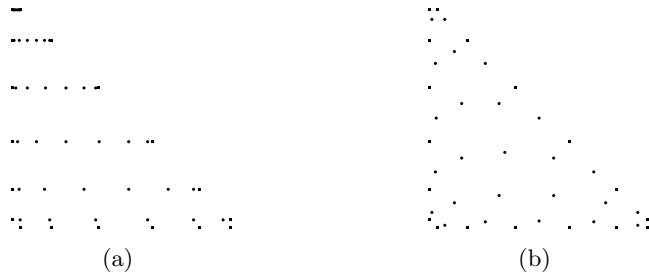
Figure 4: Gauss–Legendre (a) and Dunavant (b) interior quadrature nodes(in both cases, edge nodes are Gauss–Legendre ones).

are clustered near one vertex. Other quadrature rules, which employ a smaller number of nodes, have therefore been proposed, for instance in [49], [48] and [15]. Those rules take into account the symmetries of the element, but are generally more heuristic and nodes are not explicitly defined.

A representation of the quadrature nodes required for a spectral element approximation of degree 5 is given in Figure 4(a) and their sub-optimal distribution is quite evident.

Finally, we mention the Dunavant quadrature rules, which have been derived in [15] by solving the moment equation introduced in [29]. Nodes and weights are tabulated up to a polynomial degree of $p = 20$. We note that the number of Dunavant nodes needed to integrate exactly a polynomial of degree p is significantly lower than the corresponding number of Gaussian nodes required.

4 Dissipation, dispersion and stability analysis

Dissipation and dispersion errors play a crucial role in the overall quality of an approximation to the solution of wave propagation phenomena. Assuming that the time advancing scheme is numerically stable, a practical way to test dissipation/dispersion for a numerical scheme consists in observing the computed wave moving along a given direction for a long time in a homogeneous unbounded domain. The delay in the computed wave peaks with respect to those of the analytical one quantifies the dispersion error, whereas the decrease of the computed amplitude with respect to the amplitude of the exact solution is due to the dissipation error.

In this section, following [31], we derive the dissipation and dispersion properties of the semidiscrete and fully discrete approximation. Moreover, we investigate the numerical stability of the leap-frog scheme coupled with the proposed spatial discretization.

To this aim, we consider as analytical solution of the elastodynamics problem (1) posed on the unbounded domain Ω a travelling plane wave of unitary amplitude, i.e.,

$$\mathbf{u}(x, y, t) = e^{i(k_x x + k_y y - \omega t)}, \tag{16}$$

being $k_x = \cos\theta$ and $k_y = \sin\theta$, $\theta \in [0, 2\pi)$, the cosine directors of the wave vector $\mathbf{k} = [k_x, k_y]$. We define a triangulation $\mathcal{T}_h$ made by non-overlapping triangular elements K, having uniform size h, see Figure 5, which can be seen as a repetition of the pattern $K_c = K_1 \cup K_2$.

As usual, instead of solving on the unbounded domain Ω, we solve on Ω_c and impose periodic boundary conditions on $\partial\Omega_c$, cf. Figure 5. In this sense, we rewrite the semidiscrete
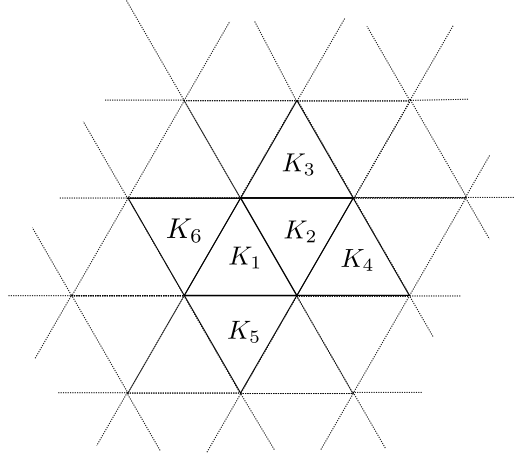
Figure 5: Element numbering for dissipation and dispersion analysis. Here, $\Omega = \mathbb{R}^2$.

DG approximation (10) in K_c,

$$\widetilde{\psi}_j(\mathbf{x}) = \begin{cases} \psi_j(\mathbf{x}) & \mathbf{x} \in K_1 \cup ... \cup K_6, \\ \mathbf{0} & \text{otherwise}, \end{cases} \qquad \widetilde{\psi}_i(\mathbf{x}) = \begin{cases} \psi_i(\mathbf{x}) & \mathbf{x} \in K_c, \\ \mathbf{0} & \text{otherwise}. \end{cases}$$

Adopting the notation of Section 3.1 and denoting by $C = J + S$, we obtain

$$M^{\ell,\ell} = \begin{pmatrix} M_1^{\ell,\ell} & 0 & 0 & 0 & 0 & 0 \\ 0 & M_2^{\ell,\ell} & 0 & 0 & 0 & 0 \end{pmatrix}, \quad \text{for } \ell = 1, 2,$$

$$A^{\ell,m} = \begin{pmatrix} A_1^{\ell,m} & 0 & 0 & 0 & 0 & 0 \\ 0 & A_2^{\ell,m} & 0 & 0 & 0 & 0 \end{pmatrix}, \quad \text{for } \ell, m = 1, 2,$$

$$C^{\ell,m} = \begin{pmatrix} C_{1,1}^{\ell,m} & C_{1,2}^{\ell,m} & 0 & 0 & C_{1,5}^{\ell,m} & C_{1,6}^{\ell,m} \\ C_{2,1}^{\ell,m} & C_{2,2}^{\ell,m} & C_{2,3}^{\ell,m} & C_{2,4}^{\ell,m} & 0 & 0 \end{pmatrix}, \quad \text{for } \ell, m = 1, 2,$$

$$\mathbf{U}^\ell = \begin{pmatrix} \mathbf{U}_1^\ell & \mathbf{U}_2^\ell & \mathbf{U}_3^\ell & \mathbf{U}_4^\ell & \mathbf{U}_5^\ell & \mathbf{U}_6^\ell \end{pmatrix}^\top, \quad \text{for } \ell = 1, 2, .$$

Applying periodic boundary conditions on ∂K_c we can easily get

$$\mathbf{U}_3 = e^{-i(hk_x/2 + \sqrt{3}hk_y/2)} \mathbf{U}_1 = \alpha_{13}\mathbf{U}_1 \quad \mathbf{U}_4 = e^{-ihk_x}\mathbf{U}_1 = \alpha_{14}\mathbf{U}_1,$$

$$\mathbf{U}_5 = e^{+i(hk_x/2 + \sqrt{3}hk_y/2)} \mathbf{U}_2 = \alpha_{25}\mathbf{U}_2 \quad \mathbf{U}_6 = e^{+ihk_x}\mathbf{U}_2 = \alpha_{26}\mathbf{U}_2.$$

Using the above relations we rewrite the problem for the reference element K_c, obtaining the following linear system

$$\widetilde{M}\ddot{\mathbf{U}} + \left(\widetilde{C} + \widetilde{A}\right)\mathbf{U} = \mathbf{0}, \tag{17}$$

where

$$\widetilde{C}_{K,J}^{\ell,m} = C_{K,J}^{\ell,m} + \sum_{I=1}^{6} \alpha_{KI} C_{K,I}^{\ell,m}$$

and $\widetilde{M}$ and $\widetilde{A}$ are the matrices M and A restricted to the triangles K_1 and K_2. Then, computing in (17) the second derivative with respect to time, we obtain

$$\left(\widetilde{C} + \widetilde{A}\right)\mathbf{U} = \Lambda \widetilde{M}\mathbf{U}, \tag{18}$$

		$\bar{e}_S$			$\bar{e}_P$		
δ	p	SIP	NIP	IIP	SIP	NIP	IIP
0.5	3	1.21e-03	4.92e-03	3.49e-03	5.61e-04	6.09e-03	4.26e-03
0.25	3	2.36e-05	2.90e-04	1.94e-04	1.41e-05	4.07e-04	2.87e-04
0.29	6	2.01e-11	8.44e-08	4.85e-08	1.17e-11	1.22e-07	8.18e-08

Table 1: $\bar{e}_S$ and $\bar{e}_P$ as a function of δ, p and $\eta = -1, 0, 1$. Penalty function defined as in (7).

		$\bar{e}_S$			$\bar{e}_P$		
δ	p	SIP	NIP	IIP	SIP	NIP	IIP
0.5	3	2.13e-03	6.86e-03	6.05e-03	4.40e-03	1.16e-02	1.28e-02
0.25	3	2.18e-05	4.46e-04	4.19e-04	2.09e-05	8.24e-04	9.32e-04
0.29	6	3.80e-11	1.36e-07	9.06e-08	2.20e-11	2.68e-07	3.13e-07

Table 2: $\bar{e}_S$ and $\bar{e}_P$ as a function of δ, p and $\eta = -1, 0, 1$. Penalty function defined as in (8).

with $\Lambda = \omega^2$. We can interpret (18) as a generalized eigenvalue problem and compute the generalized eigenvalues Λ_h that correspond to the frequencies of the travelling waves $\omega_h = \sqrt{\Lambda_h}$. Since

$$c_h = \frac{h\omega_h}{2\pi\delta} = \frac{h\sqrt{\Lambda_h}}{2\pi\delta},$$

where $\delta = p|\mathbf{k}|/2\pi$ is the number of degrees of freedom per wavelength, we can compute the velocity $c_{P,h}$ (resp. $c_{S,h}$) that is the best approximations to c_P (resp. c_S) and define $e_P := c_{P,h}/c_P - 1$ (resp. $e_S := c_{S,h}/c_S - 1$) as the compressional (resp. shear) grid dispersion error introduced by the numerical scheme.

In what follows, we will study the dependence of the dispersion error as a function of $\theta = \text{atan}(k_y/k_x)$, the order of the approximation p, the number of quadrature nodes, the choice of the Interior Penalty method (i.e. the choice of η in (5)) and different choices of penalty functions, cf. (7) and (8).

## 4.1 Semidiscrete grid dispersion error

To ease the presentation, in this section we report the semidiscrete dispersion analysis obtained choosing the boundary adapted basis functions. Very similar results have been obtained choosing the Dubiner basis functions; for brevity these results have been omitted. All simulations are performed by fixing the penalty parameter $\alpha = 10$, the Lamé parameters $\lambda = 2$, $\mu = 1$ and the mass density $\rho = 1$. This yields a wave speed ratio $c_P/c_S = 2$, which is of the same order of that usually considered in geophysical applications.

In Tables 1 and 2 we show the maximum shear and compressional grid dispersion errors, i.e., $\bar{e}_S = \max_\theta |e_S(\theta)|$ and $\bar{e}_P = \max_\theta |e_P(\theta)|$ respectively, for different choices of δ, p and different IP schemes ($\eta = -1, 0, 1$). The results reported in Table 1 have been obtained choosing the penalty function (7); analogous results obtained choosing the penalty function (8) are reported in Table 2.

It is easy to see that the SIP ($\eta = 1$) method performs uniformly better than the NIP ($\eta = -1$) and IIP ($\eta = 0$) variants, and that the grid dispersion errors resulting from the discretization that employs the penalty function (7) is uniformly smaller than the ones obtained with the penalty function (8), although being of the same order of magnitude. Moreover, as expected, increasing the polynomial order p yields a dramatic decrease in the
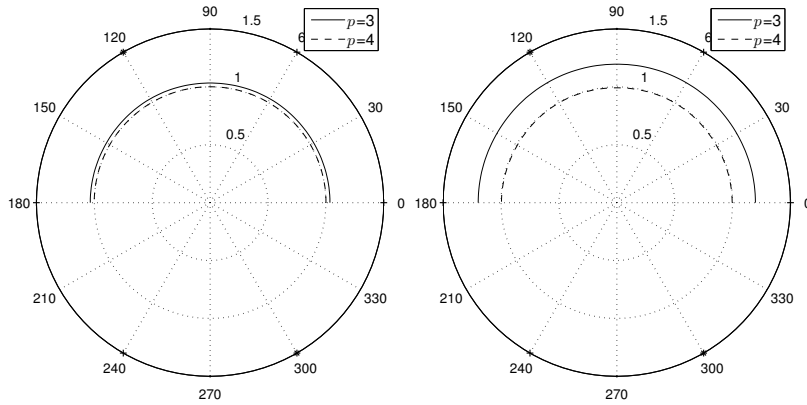
(a) Anisotropy curves $c_{S,h}/c_S$ for the SIP (left) and NIP (right) methods.
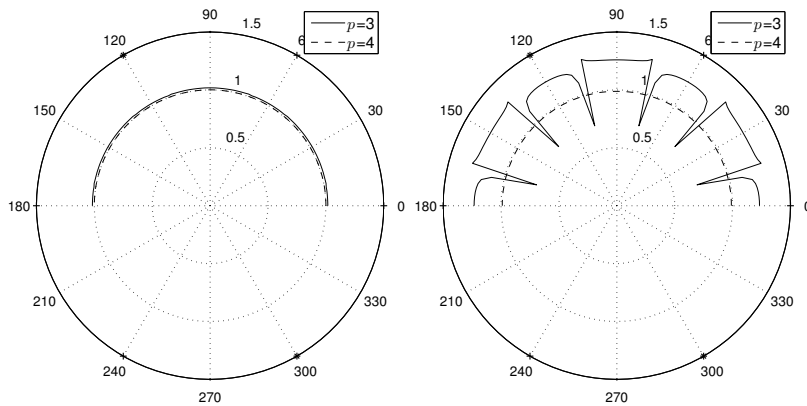
(b) Anisotropy curves $c_{P,h}/c_P$ for the SIP (left) and NIP (right) methods.

Figure 6: Anisotropy curves for $p = 3$ (-), 4 (- -) and $\alpha = 2$. Deviations from 1 magnified by a factor 100. Penalty function defined as in (7).

dispersion error.

Figure 6 displays the behaviour of the ratio between the computed speed and the exact one, i.e., $c_{S,h}/c_S$ and $c_{P,h}/c_P$ as a function of θ and p for $\eta = 1$ (SIP) and $\eta = -1$ (NIP) methods. The results obtained with the IIP method ($\eta = 0$) are either qualitatively and quantitatively similar to those of the NIP scheme. It can be observed that the SIP method tends to overestimate the real wave speed for all incident angles, i.e., $c_{S,h}/c_S$ and $c_{P,h}/c_P$ are always bigger than 1.

Finally, it is worth noting that the distortion of the mesh elements plays a crucial role in the magnitude and behaviour of the dispersion error. Indeed, Figure 7 is obtained with the SIP method and the penalty function defined as in (7) but on a mesh made of right-angled triangles. It can be seen that the dispersion error is greater for waves travelling parallel to the longest edge of the triangles. Next, we fix $\theta = \pi/4$ and consider the grid dispersion error versus the polynomial degree p. The results obtained with $\delta = 0.2$ and the SIP and NIP methods (stability function defined as in (7)) are shown in Figure 8. From these results we observe that for both methods the dispersion errors decrease exponentially to zero; the SIP method clearly outperforms the NIP scheme.

Finally, in Figure 9 we show the grid dispersion errors for $\theta = \pi/4$, as a function of the sampling ratio δ. We have an optimal order of convergence $\mathcal{O}(\delta^{2p})$ for the SIP method and a sub-optimal order of convergence $\mathcal{O}(\delta^{p+1})$ for the NIP one, as already observed in [20].
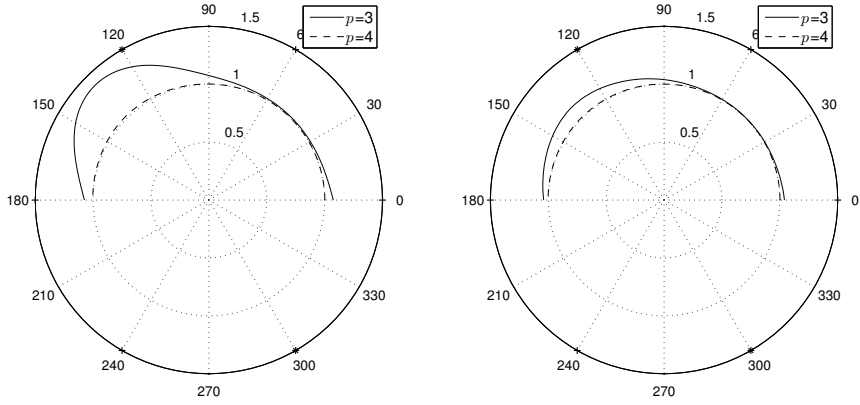
Figure 7: Anisotropy curves obtained with the SIP method ($\alpha = 2$) with the penalty function defined as in (7), on a mesh made of right-angled triangles: $c_{S,h}/c_S$ (left) and $c_{P,h}/c_P$ (right). Deviations from 1 are magnified by a factor 100.
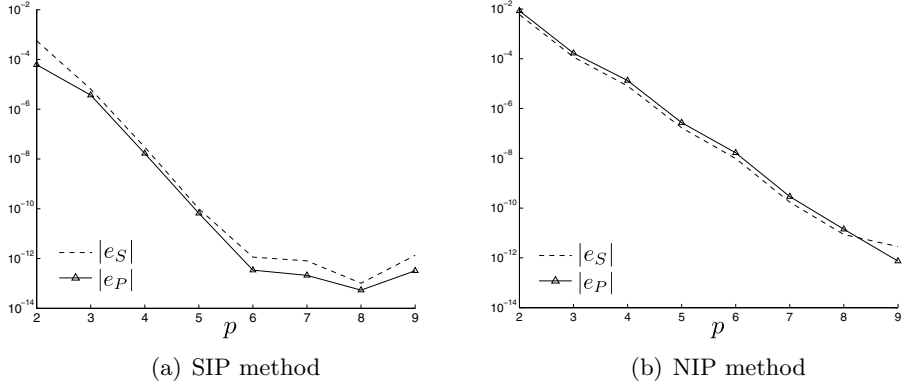

(a) SIP method

(b) NIP method

Figure 8: Grid dispersion errors $e_P(\pi/4)$ and $e_S(\pi/4)$ as a function of the polynomial degree p for the SIP (a) and NIP (b) methods. Penalty function defined as in (7): $\delta = 0.2$, $\alpha = 2$.
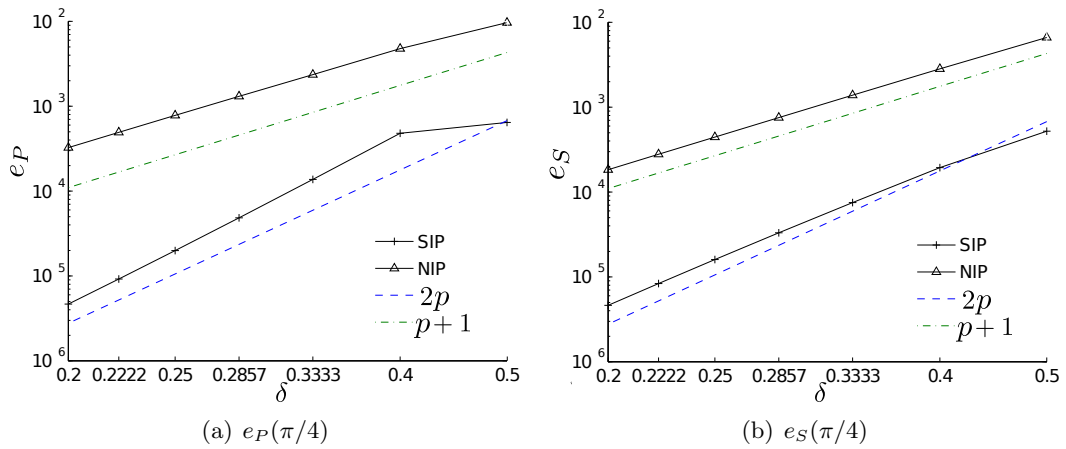

(a) $e_P(\pi/4)$

(b) $e_S(\pi/4)$

Figure 9: Grid dispersion errors versus the sampling ratio δ ($p = 3$).

13

	boundary adapted basis		Legendre-Dubiner basis	
k	$\mathrm{Im}(\omega_{S,h})$	$\mathrm{Im}(\omega_{P,h})$	$\mathrm{Im}(\omega_{S,h})$	$\mathrm{Im}(\omega_{P,h})$
2	-9.6715e-16	-4.2935e-17	-2.5416e-15	-1.5458e-15
3	2.0958e-15	4.7663e-16	2.3934e-15	8.9936e-15
4	-1.8285e-15	2.6355e-16	-1.0875e-14	-1.379e-14
5	-1.1778e-14	5.7042e-16	1.1702e-14	4.6197e-14
6	1.3079e-14	2.1062e-15	4.244e-14	-1.2404e-14
7	1.4445e-14	1.1461e-15	-1.1464e-13	-1.4941e-14
8	9.6095e-15	3.3993e-15	2.0431e-13	1.6433e-13
9	-1.5226e-14	4.9139e-15	-9.1985e-14	5.3414e-14

Table 3: Semidiscrete grid dissipation errors for the SIP method, varying the polynomial degree p and fixing $\delta = 0.2$.

4.2 Semidiscrete grid dissipation errors

To compute the grid dissipation errors, we first observe that the the amplitude of the analytic plane wave (16) is

$$|e^{i(k_x x + k_y y - \omega t)}| = e^{i\omega t},$$

being k_x and k_y real numbers. Then, we can define the grid dissipation errors as a function of time t

$$d_P := e^{\mathrm{Im}(\omega_{P,h})t}, \qquad d_S := e^{\mathrm{Im}(\omega_{S,h})t},$$

where $\omega_{P,h}$ (resp. $\omega_{S,h}$) are the approximated frequency of the shear (resp. compressional) waves. A non-dissipative scheme is thus one for which

$$\mathrm{Im}(\omega_{P,h}) = \mathrm{Im}(\omega_{S,h}) = 0,$$

for all wave vector $\mathbf{k}$. The closer to zero the above values are, the less dissipative the scheme is. The values of $\mathrm{Im}(\omega_{P,h})$ and $\mathrm{Im}(\omega_{S,h})$, computed varying the approximation degree $p = 2, \ldots, 9$ and for $\delta = 0.2$, are reported in Table 3 for the SIP method. The computed values are near machine precision and the scheme shows evidently almost irrelevant grid dissipation errors, for both sets of basis functions proposed.

4.3 Fully-discrete grid dispersion error

To analyse the dispersion error for the fully discrete approximation, we apply the leap-frog scheme to system (17) obtaining

$$\widetilde{M}\Delta t^{-2}(e^{-i\omega_h t_{n+1}} - 2e^{-i\omega_h t_n} + e^{-i\omega_h t_{n-1}})\mathbf{U}_0 = \left(\widetilde{C} + \widetilde{A}\right)e^{-i\omega_h t_n}\mathbf{U}_0,$$

or, equivalently,

$$\widetilde{M}\Delta t^{-2}(e^{-i\omega_h \Delta t} - 2 + e^{i\omega_h \Delta t})\mathbf{U}_0 = \left(\widetilde{C} + \widetilde{A}\right)\mathbf{U}_0.$$

Noting that

$$e^{-i\omega_h \Delta t} - 2 + e^{i\omega_h \Delta t} = 4\sin^2\left(\frac{\omega_h \Delta t}{2}\right),$$

we obtain a generalized eigenvalue problem of the form (18) with eigenvalues

$$\Lambda_h = \frac{4}{\Delta t^2}\sin^2\left(\frac{\omega_h \Delta t}{2}\right).$$
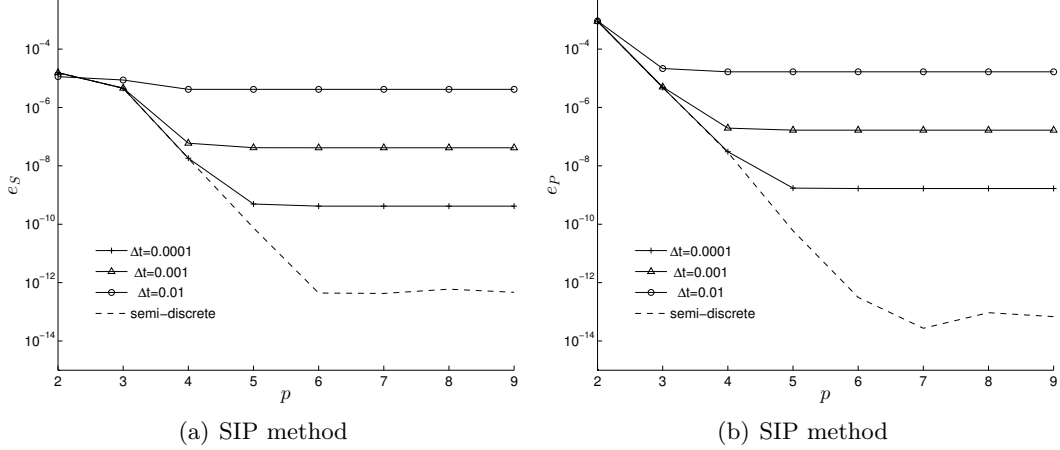
(a) SIP method   (b) SIP method

Figure 10: Fully-discrete grid dispersion errors for S-waves (a) and P-waves (b). The dashed lines represent the computed semidiscrete grid dispersion errors. We set $\Delta t = 10^{-2}, 10^{-3}, 10^{-4}$, $\delta = 0.2$ and $\theta = \pi/2$.

Then, arguing as for the semidiscrete case we can compute the approximated frequencies with the formula

$$\omega_h = \frac{2}{\Delta t} \sin^{-1}\left(\frac{\Delta t}{2}\sqrt{\Lambda_h}\right), \tag{19}$$

and denote by

$$\widetilde{e}_P := \frac{\omega_{P,h}}{\omega_P} - 1, \qquad \widetilde{e}_S := \frac{\omega_{S,h}}{\omega_S} - 1,$$

the fully-discrete compressional and shear dispersion error respectively. Notice that, for a sufficiently small Δt, the right hand side in (19) can be expanded as a Taylor series giving

$$\omega_h \sim \sqrt{\Lambda_h} + \mathcal{O}\left(\Delta t^2\right).$$

Then, we expect the semidiscrete error to be dominant until it reaches a threshold $\sim C\Delta t^2$ with $C > 0$ and the error due to the time discretization to be dominant afterwards. In Figure 10 we fix $\theta = \pi/4$, $\delta = 0.2$ and report the computed errors $\widetilde{e}_P$ and $\widetilde{e}_S$ as a function of $p = 2, \ldots, 9$, for different choices of $\Delta t = 10^{-2}, 10^{-3}, 10^{-4}$. For the sake of comparison, the results are compared with the analogous semidiscrete ones. As expected, for $\Delta t \to 0$ the fully-discrete grid dispersion errors tend to the semidiscrete ones.

4.4 Numerical stability of the fully-discrete approximation

In this section, following [3] we analyze the stability properties of the proposed fully-discrete numerical approximation. We use the same parameters as in the previous section, that is, we fix the penalty parameter $\alpha = 10$, the Lamé parameters $\lambda = 2, \mu = 1$ and the mass density $\rho = 1$. Moreover we set $\delta = 0.2$ and $\theta = \pi/4$. Note that for lower ratios c_P/c_S the stability requirement would be stricter, but that with this ratio we are able to discriminate between the two stability functions.

In the same configuration as the one shown in Figure 5, we consider the generalized eigenvalue problem (18), i.e.,

$$\left(\widetilde{C} + \widetilde{A}\right)\mathbf{U} = \Lambda\widetilde{M}\mathbf{U}.$$
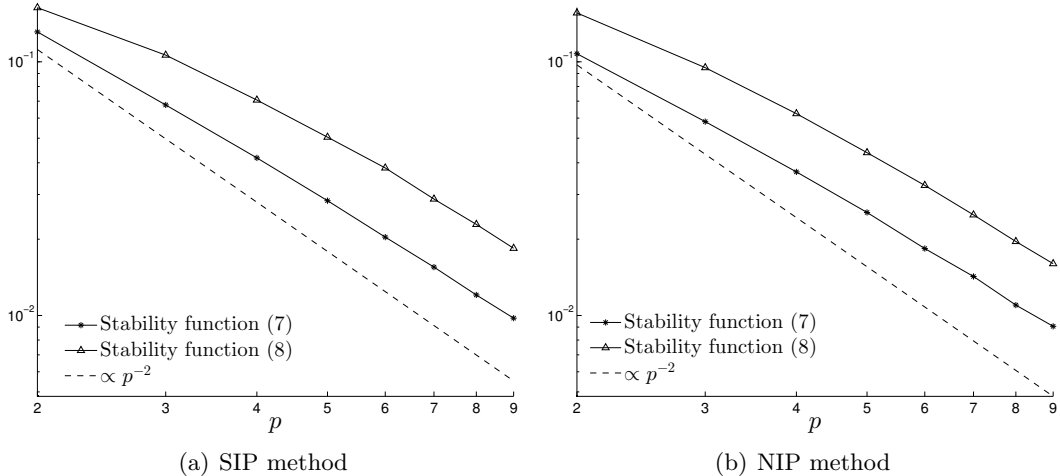
15

Figure 11: Stability parameter as a function of the polynomial degree p, for both the stability functions defined as in (7) and (8).

In order to make the dependence of $\widetilde{C} + \widetilde{A}$ on both the mesh size h and the polynomial approximation degree p explicit, we rewrite the above system with elements edges length equal to 2, getting

$$\Lambda = \left(\frac{h}{\Delta t}\right)^2 \sin^2\left(\frac{\omega_h \Delta t}{2}\right).$$

Now, defining the stability parameter $q = c_P \Delta t / h$, we can deduce that

$$q\sqrt{\Lambda} = c_P \sin\left(\frac{\omega_h \Delta t}{2}\right),$$

and then we can express the CFL condition (13) as

$$q \leq \frac{c_p}{\sqrt{\Lambda}} = C_{CFL}(\Lambda),$$

with $0 < C_{CFL} \leq 1$. Since the above relation must hold for any eigenvalue of the system (18), in particular, it has to be verified for $\max_{j,\theta} \Lambda_j(\theta)$. Then, by numerically computing this quantity, we can investigate the numerical stability of the DG scheme. In Figure 11, we plot the stability parameter q versus the polynomial approximation degree p, for the SIP method with the different choices of the penalty function (cf. (7) and (8)). The results show that $q \sim p^{-2}$, in agreement with [2, 3]. We can also observe that the stability function (8) provides less restrictive bounds than using (7), but this comes at the price of a larger dispersion error, as already shown in Section 4.1. Moreover, we observe that the NIP method has more restrictive stability bounds than the SIP scheme when coupled with the leap-frog scheme, without any gain in accuracy. This is in agreement with [3] where a similar analysis is derived for dGSE methods for tensor-product meshes. Finally, it is worth noting that those values constitute only a necessary bound, though it has been found to be sufficient in practice [12].

5   Numerical results

In this section we test the performance of our dGSEM on simplicial elements on classical benchmark as well as on realistic seismic wave propagation problems.

16

In order to study the convergence properties, we define on the space $\boldsymbol{V}^h$ the mesh dependent norm

$$||\mathbf{u}||_{\boldsymbol{V}^h}^2 := \sum_{K \in \mathcal{T}_h} ||\mathbb{C}^{1/2}\varepsilon(\mathbf{u})||_{0,K}^2 + \sum_{e \in \mathcal{E}} ||\mathbb{S}_e^{1/2}[\![\mathbf{u}]\!]||_{0,e}^2, \quad \forall \, \mathbf{u} \in \boldsymbol{V}^h$$

and the time dependent norm

$$||\mathbf{u}||_{L^2((0,T];\boldsymbol{V})} := \left(\int_0^T ||\mathbf{u}(t)||_{\boldsymbol{V}}^2 \mathrm{d}t \right)^{\frac{1}{2}},$$

where $\boldsymbol{V}$ can be either $\boldsymbol{V} = \boldsymbol{L}^2(\Omega)$ or $\boldsymbol{V} = \boldsymbol{V}^h$.

Example 1

For the first test case, we consider the domain $\Omega = (-1/2, 1/2) \times (0, 1)$ and we set the body force $\mathbf{f}$, the initial and boundary conditions such that

$$\mathbf{u}_{ex}(x, y, t) = \cos(t) \begin{pmatrix} \sin(\pi x)\sin(\pi y) \\ \cos(\pi x)\cos(\pi y) \end{pmatrix}$$

is the exact solution to problem (1). The corresponding numerical approximation $\mathbf{u}_h$ is computed considering the SIP approximation with the stability function defined as in (7), due to its best dispersion properties (cf. Section 4.1).

In Figure 12(a) we plot the $L^2\left((0,T]; \boldsymbol{L}^2(\Omega)\right)$ and $L^2\left((0,T]; \boldsymbol{V}^h\right)$ norms of the error as a function of the polynomial degree p. These results have been obtained employing a structured mesh made by 32 right-angled triangles, setting $T = 1$ and $\Delta t = 5 \cdot 10^{-4}$. We observe that the $L^2\left(\cdot; \boldsymbol{V}^h\right)$ error is consistently two orders of magnitude bigger than the $L^2\left(\cdot; L^2\right)$ error, but the behaviour with respect to p is qualitatively the same. Specifically, the convergence of the numerical solution to the analytical one is exponential.

In Figure 12(b) the computed errors are plotted versus the mesh size h. These results have been obtained on a structured mesh with $n_{el} = 32, 72, 128, 200$ triangles so that the size of the catheti of the elements takes the values $h = 1/4, 1/6, 1/8, 1/10$. As expected, the error converges to zero as h^{p+1}.

The Lamb's problem

We next consider Lamb's problem [28], which involves the propagation of seismic waves in an elastic half plane, due to a point source located just below the surface and imposing null stress conditions on the surface. The elastic domain Ω is a rectangle of width 4000 m and height 2000 m, with mass density $\rho = 2000$ Kg/m^3, $c_P = 3200$ m/s and $c_S = 1847.5$ m/s. A point source is located at $\mathbf{p}_f = (1500, 1950)$ m, 50 meters below the free surface and it is modulated in time as the Ricker wavelet

$$\mathbf{f}(\mathbf{x}, t) = \left(1 - 2(f_m \pi)^2(t - t_0)^2\right) e^{-(f_m \pi)^2(t - t_0)^2} \delta_0(\mathbf{x} - \mathbf{p}_f), \tag{20}$$

where $\delta_0(\cdot)$ is the Dirac distribution and f_m (resp. t_0) is a frequency (resp. time delay) to be specified. Two receivers r_1 and r_2 are located respectively at the points $r_1 = (2200, 2000)$ m and $r_2 = (2700, 2000)$ m. Figure 13 provides a close up of the physical phenomenon: after the source activation, there is a P-wave travelling towards the bottom of the domain, followed by an S-wave travelling almost horizontally. At the top edge of the domain, the Rayleigh wave is clearly visible. In Figure 14 we show the computed displacements obtained with $h = 50, p = 5, \Delta t = 2.5 \cdot 10^{-4}$ s and fixing $f_m = 10$ Hz and $t_0 = 0.1$ s for the Ricker
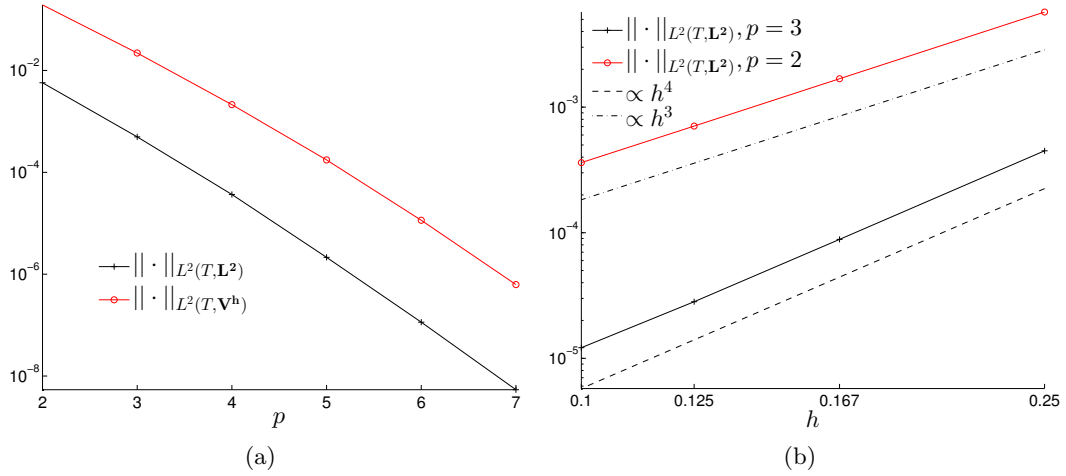
17

Figure 12: Example 1: computed errors versus the polynomial degree $p = 2, ..., 7$, for $h = 1/4$ (left); computed error versus mesh size h for $p = 2, 3$ (right).
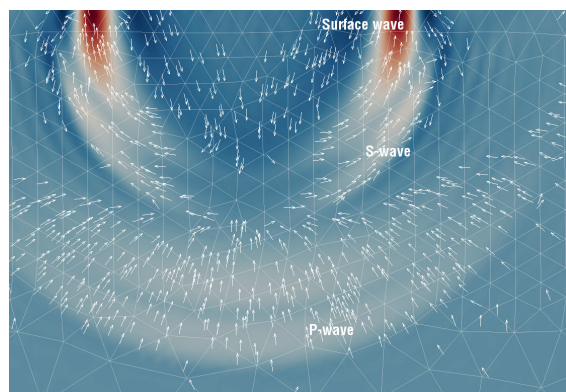

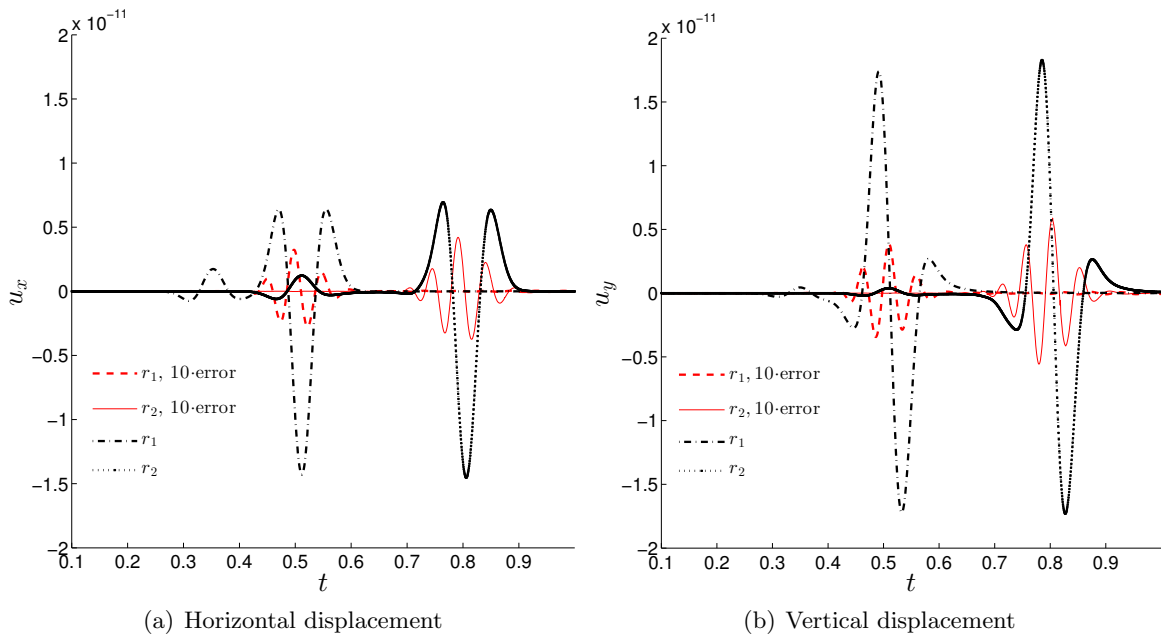Figure 13: Lamb's problem: close up of the waves propagating away from the point source.

18

(a) Horizontal displacement   (b) Vertical displacement

Figure 14: Lamb's problem: computed displacements and errors (magnified by a factor of 10) registered at the receivers r_1 and r_2. SIP method with $\alpha = 10$.

Material	c_P [m/s]	c_S [m/s]	ρ [kg/m^3]
I	2500	1250	2000
II	4000	2000	2200

Table 4: Elastic wedge problem: properties of the materials.

wavelet (20). For the Lamb's problem, we are able to recover the analytical structure of the surface wave (via the EX2DDIR software [7]). The difference between the analytical and the numerical solution is also shown, magnified by a factor of 10. Notice that the main event recorded by the receivers is the transit of the surface wave. It is furthermore interesting to compare the computed surface wave speed with the exact one. The temporal distance between the peaks recorded by the receivers r_1 and r_2 in Figure 14(b) (computed at the available time steps) is $\delta t \simeq 0.294 \pm 0.001$ s. Then, considering the distance between the receivers, we get an empirical speed $c_{h,\mathrm{surf}} \simeq 1700 \pm 6$ m/s, while a direct (analytical) calculation of the surface wave-speed gives $c_{\mathrm{surf}} \simeq 1698.6$ m/s. Therefore, the error is clearly below the temporal resolution of the approximation.

The elastic wedge problem

In the elastic wedge problem the propagation of a surface wave in a square domain divided by its diagonal into two different materials is considered. Here, we set up the material properties as in Table 4. Specifically, material I (resp. material II) occupies the top-left (resp. bottom-right) side of the square. We set a Rayleigh wave as the initial data of system (1) and Neumann boundary conditions are imposed on $\partial\Omega$. The Rayleigh wave is analitically computed in a half space with the properties of Material I.

We have considered the grid depicted in Figure 15; such a choice allows for a constant number of degrees of freedom per wavelength. In particular, the results presented have been computed with approximately 5 degrees of freedom per wavelength. The set up of
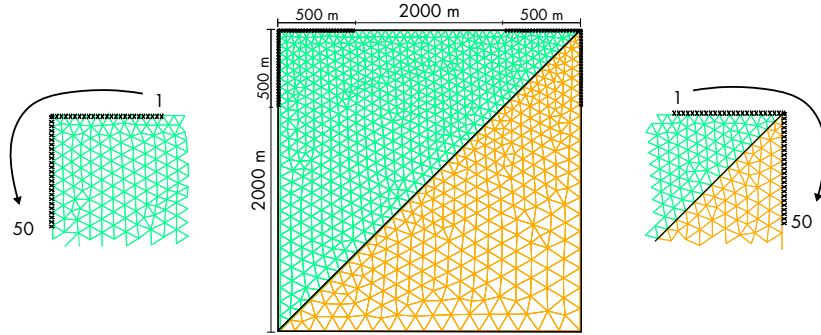
19

Figure 15: Elastic wedge problem: domain, mesh, receivers (shown in bold lines at corners) and zoom of receivers numbering at the corners.

the receivers and the mesh are shown in Figure 15: the domain is a square of edge length 2000 m, while the 100 receivers are located at the two top corners, spanning 500 meters both on the top and lateral edges.

In Figures 16 and 17 we report the approximated solution recorded by the receivers placed on the corners of the domain (see Figure 15). Here, we use $p = 8$, $\Delta t = 5 \cdot 10^{-5}$ s and a final observation time $T = 1.5$. We employed the SIP method with the stability function defined as in (8), with $\alpha = 10$. In the homogeneous corner (Figure 17) the effect of the transmitted Rayleigh wave travelling downwards and of the reflected wave travelling backwards is clearly visible.

On the other hand, in the heterogeneous corner, as expected, the reflected wave is evident, while the transmitted one if of definitely inferior amplitude. The difference in speed between the reflected and the transmitted surface wave is also observable, in agreement with [32].

6   Conclusions and perspectives

We have implemented and analyzed a discontinuous Galerkin spectral element approximation of the elastodynamics equation on meshes made of simplicial elements.

We were particularly interested in the simulation of wave propagation phenomena and therefore concerned by the dissipation and dispersion errors introduced by the method. The results we obtained show that the method introduces very low dissipation and that its dispersion error converges exponentially to machine precision with respect to the polynomial order p. The approximation is also exponentially convergent to the solution (in the standard norms and with respect to p) in the case of the model problem with analytical exact solution. In general, the quality of the approximation is comparable with that obtained on tensor product grids. Furthermore, when applied to realistic cases, the scheme accurately captures phenomena such as the formation and propagation of surface waves and the differences in propagation speed for heterogeneous materials.

On the other hand, the constraints on the stability of the method are stricter than in the tensor product case; additionally, a tensor product discrete space allows for more computational efficiency. Since the discontinuous nature of the scheme gives the possibility to easily combine multiple shapes in the same grid and allows for hanging nodes, a scheme built on meshes composed by elements of different shapes is advisable. With such a scheme, either the efficiency of tensor product methods and the flexibility of simplicial elements can be exploited.
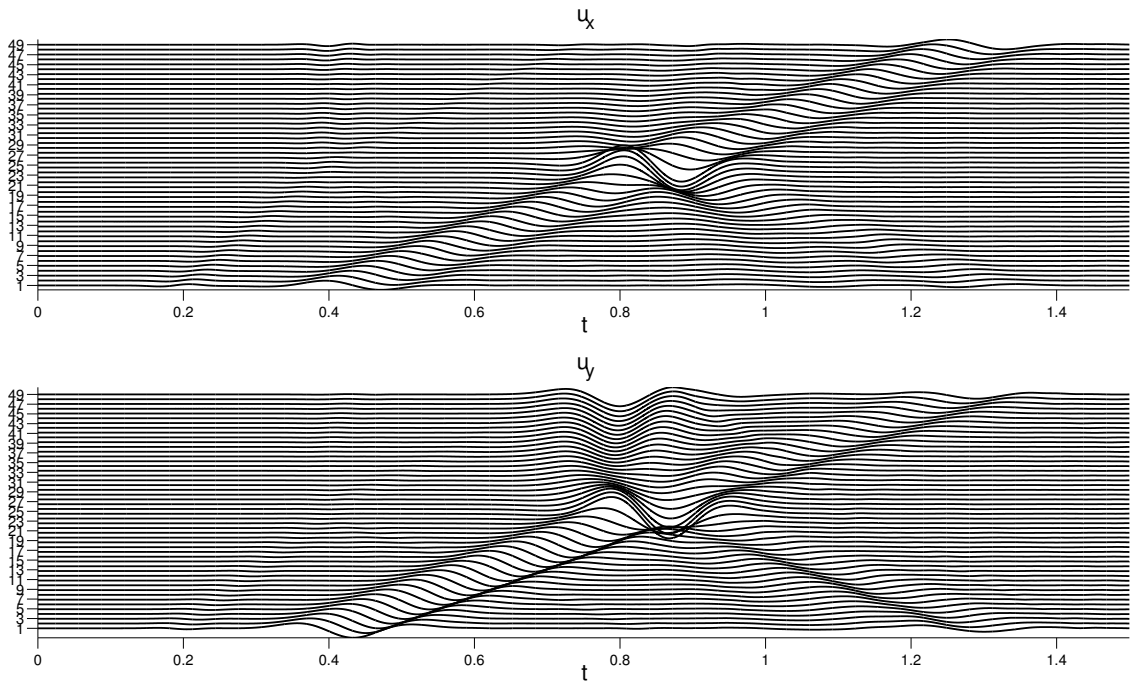
Figure 16: Seismograms at the top left (homogeneous) corner (cf. Figure 15). Horizontal (above) and vertical (below) components of the discrete displacement. Time is on the x-axis, the receiver numbers are shown on the y-axis. SIP method with $\alpha = 10$.
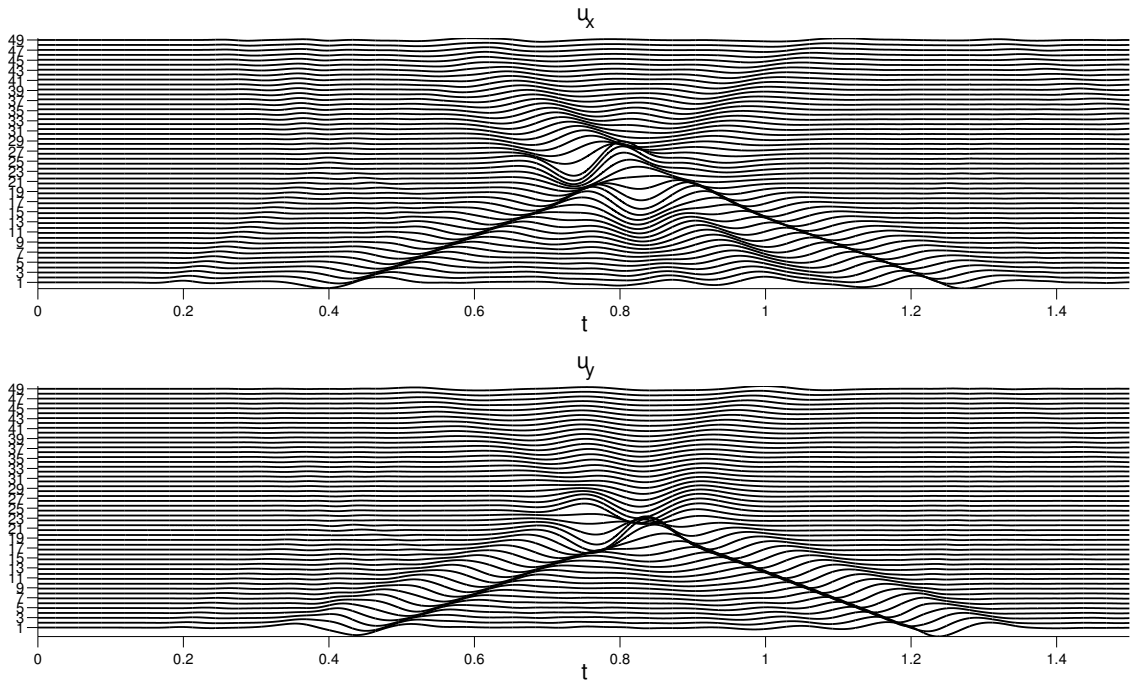

Figure 17: Seismograms at the top right (heterogeneous) corner (cf. Figure 15). Horizontal (above) and vertical (below) components of the discrete displacement. Time is on the x-axis, the receiver numbers are shown on the y-axis. SIP method with $\alpha = 10$.

References

[1] R. A. Adams and J. J. F. Fournier. *Sobolev spaces*, volume 140 of *Pure and Applied Mathematics*. Elsevier/Academic Press, Amsterdam, second edition, 2003.

[2] P. F. Antonietti and P. Houston. A class of domain decomposition preconditioners for *hp*-discontinuous Galerkin finite element methods. *J. Sci. Comput.*, 46(1):124–149, 2011.

[3] P. F. Antonietti, I. Mazzieri, A. Quarteroni, and F. Rapetti. Non-conforming high order approximations of the elastodynamics equation. *Comput. Methods Appl. Mech. Engrg.*, 209/212:212–238, 2012.

[4] D. N. Arnold. An interior penalty finite element method with discontinuous elements. *SIAM J. Numer. Anal.*, 19(4):742–760, 1982.

[5] D. N. Arnold, F. Brezzi, B. Cockburn, and L. D. Marini. Unified analysis of discontinuous Galerkin methods for elliptic problems. *SIAM J. Numer. Anal.*, 39(5):1749–1779, 2001/02.

[6] B. Ayuso de Dios, P. F. Antonietti, I. Mazzieri, and A. Quarteroni. Stability analysis for discontinuous galerkin approximations of the elastodynamics problem. *MOX-Report*, 56/2013, 2013.

[7] P. Berg, F. If, P. Nielsen, and O. Skovgaard. Analytical reference solutions. *Modeling the earth for oil exploration*, pages 421–427, 1994.

[8] L. Bos, M. A. Taylor, and B. A. Wingate. Tensor product Gauss-Lobatto points are Fekete points for the cube. *Math. Comp.*, 70(236):1543–1547, 2001.

[9] C. Canuto, M. Y. Hussaini, A. Quarteroni, and T. A. Zang. *Spectral methods. Fundamentals in single domains*. Scientific Computation. Springer, Berlin, 2006.

[10] C. Canuto, M. Y. Hussaini, A. Quarteroni, and T. A. Zang. *Spectral methods. Evolution to complex geometries and applications to fluid dynamics*. Scientific Computation. Springer, Berlin, 2007.

[11] R. Courant, K. Friedrichs, and H. Lewy. Über die partiellen Differenzengleichungen der mathematischen Physik. *Math. Ann.*, 100(1):32–74, 1928.

[12] J. D. De Basabe and M. K. Sen. Stability of the high-order finite elements for acoustic or elastic wave propagation with high-order time stepping. *Geophys. J. Int.*, 181(1):577–590, 2010.

[13] J. Douglas, Jr. and T. Dupont. Interior penalty procedures for elliptic and parabolic Galerkin methods. In *Computing methods in applied sciences (Second Internat. Sympos., Versailles, 1975)*, pages 207–216. Lecture Notes in Phys., Vol. 58. Springer, Berlin, 1976.

[14] M. Dubiner. Spectral methods on triangles and other domains. *J. Sci. Comput.*, 6(4):345–390, 1991.

[15] D. A. Dunavant. High degree efficient symmetrical Gaussian quadrature rules for the triangle. *Internat. J. Numer. Methods Engrg.*, 21(6):1129–1148, 1985.

[16] E. Faccioli, F. Maggio, R. Paolucci, and A. Quarteroni. 2d and 3d elastic wave propagation by a pseudo-spectral domain decomposition method. *Journal of Seismology*, 1(3):237–251, 1997.

[17] G. J. Gassner, F. Lörcher, C.-D. Munz, and J. S. Hesthaven. Polymorphic nodal elements and their application in discontinuous Galerkin methods. *J. Comput. Phys.*, 228(5):1573–1590, 2009.

[18] E. H. Georgoulis, E. Hall, and P. Houston. Discontinuous Galerkin methods on *hp*-anisotropic meshes. I. A priori error analysis. *Int. J. Comput. Sci. Math.*, 1(2-4):221–244, 2007.

[19] E. H. Georgoulis, E. Hall, and P. Houston. Discontinuous Galerkin methods for advection-diffusion-reaction problems on anisotropically refined meshes. *SIAM J. Sci. Comput.*, 30(1):246–271, 2007/08.

[20] K. Harriman, P. Houston, B. Senior, and E. Süli. *hp*-version discontinuous Galerkin methods with interior penalty for partial differential equations with nonnegative characteristic form. In *Recent advances in scientific computing and partial differential equations (Hong Kong, 2002)*, volume 330 of *Contemp. Math.*, pages 89–119. Amer. Math. Soc., Providence, RI, 2003.

[21] J. S. Hesthaven. From electrostatics to almost optimal nodal sets for polynomial interpolation in a simplex. *SIAM J. Numer. Anal.*, 35(2):655–676, 1998.

[22] J. S. Hesthaven and C.-H. Teng. Stable spectral methods on tetrahedral elements. *Siam Journal on Scientific Computing*, 21(6):2352–2380, 2000.

[23] J. S. Hesthaven and T. Warburton. *Nodal discontinuous Galerkin methods*, volume 54 of *Texts in Applied Mathematics*. Springer, New York, 2008.

[24] G. E. Karniadakis and S. J. Sherwin. *Spectral/hp element methods for computational fluid dynamics*. Numerical Mathematics and Scientific Computation. Oxford University Press, New York, second edition, 2005.

[25] A. Klöckner, T. Warburton, J. Bridge, and J. S. Hesthaven. Nodal discontinuous Galerkin methods on graphics processors. *J. Comput. Phys.*, 228(21):7863–7882, 2009.

[26] D. Komatitsch and J. Tromp. Spectral-element simulations of global seismic wave propagation-i. validation. *Geophys. J. Int.*, 149(2):390–412, 2002.

[27] T. Koornwinder. Two-variable analogues of the classical orthogonal polynomials. In *Theory and application of special functions (Proc. Advanced Sem., Math. Res. Center, Univ. Wisconsin, Madison, Wis., 1975)*, pages 435–495. Math. Res. Center, Univ. Wisconsin, Publ. No. 35. Academic Press, New York, 1975.

[28] H. Lamb. On the propagation of tremors over the surface of an elastic solid. *Philosophical Transactions of the Royal Society of London. Series A, Containing Papers of a Mathematical or Physical Character*, 203:pp. 1–42, 1904.

[29] J. N. Lyness and D. Jespersen. Moderate degree symmetric quadrature rules for the triangle. *J. Inst. Math. Appl.*, 15:19–32, 1975.

[30] I. Mazzieri. *Non-conforming high order methods for the elastodynamics equation*. PhD thesis, Politecnico di Milano, 2012.

[31] I. Mazzieri and F. Rapetti. Dispersion analysis of triangle-based spectral element methods for elastic wave propagation. *Numer. Algorithms*, 60(4):631–650, 2012.

[32] E. D. Mercerat, J.-P. Vilotte, and F. J. Sánchez-Sesma. Triangular spectral element simulation of two-dimensional elastic wave propagation using unstructured triangular grids. *Geophys. J. Int.*, 166(2):679–698, 2006.

[33] R. Pasquetti and F. Rapetti. Spectral element methods on unstructured meshes: which interpolation points? *Numer. Algorithms*, 55(2-3):349–366, 2010.

[34] A. T. Patera. A spectral element method for fluid dynamics: Laminar flow in a channel expansion. *J. Comput. Phys.*, 54(3):468 – 488, 1984.

[35] C. Pelties, J. de la Puente, J.-P. Ampuero, G. B. Brietzke, and M. Käser. Three-dimensional dynamic rupture simulation with a high-order discontinuous galerkin method on unstructured tetrahedral meshes. *Journal of Geophysical Research: Solid Earth*, 117(B2), 2012.

[36] D. Peter, D. Komatitsch, Y. Luo, R. Martin, N. Le Goff, E. Casarotti, P. Le Loher, F. Magnoni, Q. Liu, C. Blitz, T. Nissen-Meyer, P. Basini, and J. Tromp. Forward and adjoint simulations of seismic wave propagation on fully unstructured hexahedral meshes. *Geophys. J. Int.*, 186(2):721–739, 2011.

[37] A. Quarteroni, R. Sacco, and F. Saleri. *Numerical mathematics*, volume 37 of *Texts in Applied Mathematics*. Springer, Berlin, second edition, 2007.

[38] F. Rapetti, A. Sommariva, and M. Vianello. On the generation of symmetric lebesgue-like points in the triangle. *Journal of Computational and Applied Mathematics*, 236(18):4925–4932, 2012.

[39] P.-A. Raviart and J.-M. Thomas. *Introduction à l'analyse numérique des équations aux dérivées partielles*. Collection Mathématiques Appliquées pour la Maîtrise. Masson, Paris, 1983.

[40] W. H. Reed and T. R. Hill. Triangular mesh methods for the neutron transport equation. Technical Report LA-UR-73-479, Los Alamos Scientific Laboratory, 1973.

[41] B. Rivière and M. F. Wheeler. Discontinuous finite element methods for acoustic and elastic wave problems. In *Current trends in scientific computing (Xi'an, 2002)*, volume 329 of *Contemp. Math.*, pages 271–282. Amer. Math. Soc., Providence, RI, 2003.

[42] B. Rivière, M. F. Wheeler, and V. Girault. Improved energy estimates for interior penalty, constrained and discontinuous Galerkin methods for elliptic problems. I. *Comput. Geosci.*, 3(3-4):337–360 (2000), 1999.

[43] B. N. Ryland and H. Z. Munthe-Kaas. On multivariate Chebyshev polynomials and spectral approximations on triangles. In *Spectral and High Order Methods for Partial Differential Equations*, pages 19–41. Springer, 2011.

[44] G. Seriani, E. Priolo, and A. Pregarz. Modelling waves in anisotropic media by a spectral element method. *Proceedings of the third international conference on mathematical and numerical aspects of wave propagation*, pages 289–298, 1995.

[45] S. J. Sherwin and G. E. Karniadakis. A new triangular and tetrahedral basis for high-order (*hp*) finite element methods. *Internat. J. Numer. Methods Engrg.*, 38(22):3775–3802, 1995.

[46] M. Stupazzini, R. Paolucci, and H. Igel. Near-fault earthquake ground-motion simulation in the grenoble valley by a high-performance spectral element code. *Bull. Seismol. Soc. Am.*, 99(1):286–301, 2009.

[47] G. Szegő. *Orthogonal polynomials.* American Mathematical Society, Providence, R.I., fourth edition, 1975. American Mathematical Society, Colloquium Publications, Vol. XXIII.

[48] M. A. Taylor, B. A. Wingate, and L. P. Bos. A cardinal function algorithm for computing multivariate quadrature points. *SIAM J. Numer. Anal.*, 45(1):193–205 (electronic), 2007.

[49] S. Wandzura and H. Xiao. Symmetric quadrature rules on a triangle. *Comput. Math. Appl.*, 45(12):1829–1840, 2003.

[50] T. Warburton. An explicit construction of interpolation nodes on the simplex. *Journal of Engineering Mathematics*, 56(3):247–262, 2006.

[51] M. F. Wheeler. An elliptic collocation-finite element method with interior penalties. *SIAM J. Numer. Anal.*, 15(1):152–161, 1978.

MOX Technical Reports, last issues

Dipartimento di Matematica
Politecnico di Milano, Via Bonardi 9 - 20133 Milano (Italy)

10/2015   Antonietti, P. F.; Grasselli, M.; Stangalino, S.; Verani, M.
Discontinuous Galerkin approximation of linear parabolic problems with dynamic boundary conditions

06/2015   Perotto, S.; Zilio, A.
Space-time adaptive hierarchical model reduction for parabolic equations

09/2015   Ghiglietti, A.; Ieva, F.; Paganoni, A.M.; Aletti, G.
On linear regression models in infinite dimensional spaces with scalar response

07/2015   Giovanardi, B.; Scotti, A.; Formaggia, L.; Ruffo, P.
A general framework for the simulation of geochemical compaction

08/2015   Agosti, A.; Formaggia, L.; Giovanardi, B.; Scotti, A.
Numerical simulation of geochemical compaction with discontinuous reactions

05/2015   Chen, P.; Quarteroni, A.; Rozza, G.
Reduced order methods for uncertainty quantification problems

4/2015   Arioli, G.; Gazzola, F.
On a nonlinear nonlocal hyperbolic system modeling suspension bridges

1/2015   Pini, A.; Stamm, A.; Vantini, S.
Hotelling s T^2 in functional Hilbert spaces

2/2015   Menafoglio, A.; Petris, G.
Kriging for Hilbert-space valued random fields: the Operatorial point of view

3/2015   Abramowicz, K.; de Luna, S.; Häger, C.; Pini, A.; Schelin, L.; Vantini, S.
Distribution-Free Interval-Wise Inference for Functional-on-Scalar Linear Models